# Multimodal Information Structuring with Single Layer Soft Skins and High-Density Electrical Impedance Tomography

David Hardman,[1*] Thomas George Thuruthel,[2], Fumiya Iida[1]

[1]Bio-Inspired Robotics Lab, University of Cambridge, UK
[2]Department of Computer Science, University College London, UK

[*]To whom correspondence should be addressed; E-mail: dsh46@cam.ac.uk.

**The human skin can reliably capture a wide range of multimodal data over a large surface while providing a soft interface. Artificial technologies using MEMS can emulate these biological functions but present numerous challenges in fabrication, delamination due to soft-rigid interfaces, and electrical interference. To address these difficulties, we present a single layer multimodal sensory skin made using only a highly sensitive hydrogel membrane. Using electrical impedance tomography techniques, we access up to 863,040 conductive pathways across the membrane, allowing us to identify at least six distinct types of multimodal stimuli, including human touch, damage, multipoint insulated presses, and local heating. Through comprehensive physical testing, we demonstrate that the highly redundant and coupled sensory information from these pathways can be structured using data-driven techniques, selecting which path-**

**ways should be monitored for efficient multimodal perception. To demonstrate our approach's versatility, we cast the hydrogel into the shape and size of an adult human hand. Using our information structuring strategy, we demonstrate the hand's ability to predict environmental conditions, localize human touch, and generate proprioceptive data. Our framework addresses the challenge of physically extracting meaningful information in multimodal soft sensing, opening new directions for the information-led design of single layer skins in sensitive systems.**

**Summary:** High-density impedance measurements are used to monitor multimodal stimuli from single layer skins over a hollow 3D hand.

# Introduction

Human skin provides us with a large amount and variety of sensory information. Creating similar artificial skins for robotic systems is challenging not only in the physical design space but also at the computational level (*1–4*). Many skins and soft sensing interfaces have been designed to respond to light contact (*5–10*). Such single-modality sensing is essential for robots to perform complex tasks (*11*), but does not capture the full functionality of human skins — such as temperature, pressure, and damage sensing. As we design more functional robots, the need for multimodal perception in soft skins continues to grow (*12*).

Electronic skins transform physical information into electronic signals using a combination of functional materials, mechanisms, and device architectures (*13–15*). Multimodality is typically obtained by combining sensing units with stimuli-specific responses (*16, 17*);

many existing robotic skins rely on the integration of modular sensory components embedded in a flexible/soft substrate (*18–25*). However, while such skins show promise as wearable sensing technologies, they are still not well-suited for robotic applications for several reasons. Firstly, their fabrication is tedious due to the need to distribute and wire multiple small components over a large surface, limiting them to simple shapes. Due to the presence of multiple soft-rigid interfaces, the skins are typically not stretchable or are highly prone to damage. Finally, there is the challenge of signal interference and cross-talk, which reduces accuracy (*12, 26*).

Another technique for measuring multimodal sensory information, which is rarely found in literature, is to use the same sensing unit for all stimuli, with different responses corresponding to different stimuli. This approach presents challenges in decoupling the corresponding stimuli, but vastly simplifies fabrication and uses fewer soft/rigid interfaces. Decoupling and distinguishing the external stimuli is then achieved using high-throughput sensory channels and computational techniques that exploit redundancies in information (*27, 28*). Vision-based tactile skins are one such sensing mechanism that allows high-density sensory information, which can be used for multimodal perception (*27, 29, 30*). However, vision-based sensors are limited to simple shapes and are prone to damage due to soft-rigid interfaces (refer to Table S2 for a comparison of the state-of-the-art tactile skins).

Recently, electrical impedance tomography (EIT) has emerged as a method for sensorizing continuous conductive materials like fabrics and hydrogels (*31–37*). Electrodes are positioned over the material or around its perimeter, and selected tetrapolar electrode configurations are used for multiplexed impedance measurements. With increasing electrode count, numerous configurations arise. By selecting configurations based on the generated electric fields across soft skin, the method's output can be structured, balanc-

ing sampling rate and information content (*38, 39*). Traditionally, electrode selection has depended on analytic reconstruction methods, but with the rise of machine learning in sensory data processing (*35, 40*), more possibilities are available.

Previous works have explored data-driven selection of EIT drive electrodes, often considering adjacent, opposite, and trigonometric configurations (*34, 41, 42*), mainly through simulation-based analyses (*43, 44*). Direct physical testing can identify excitation patterns better suited to the application (*45*), without Sim2Real discrepancies. However, physical experiments are more time consuming than their simulated equivalents. By comparing the information returned from every possible electrode configuration in our physical sensory system, we employ a data-driven approach to return multimodal data with the maximum information content. By monitoring all possibilities, we can identify which configurations provide the most information about particular sensory stimuli, enabling efficiency in subsequent system implementations by monitoring only these channels. We focus on techniques which can be directly applied to a range of complex-shaped multimodal skins without the need for finite element simulations. Although traditional EIT solvers first aim to reconstruct a system's conductivity map, we instead output the sensory stimuli directly: type, location, temperature, and humidity.

By monitoring every configuration, we are not limited by the traditional assumptions of reciprocity, measurement interdependence, and frequency independence (*46*), and we are instead able to directly identify a system's optimal configurations for specific sensing modalities. Such an approach allows for complex physical setups in which these assumptions may not hold perfectly; even when they do, our data-driven approach can exploit the subsequent information redundancies to generate its predictions from noisy data sources, operating close to idealized limits of information content.

A limited number of works have explored the application of EIT for multimodal robotic

sensing: including applications for human touch, temperature sensing, and gesture recognition (*31, 47, 48*). We have previously shown that a circular 2D skin trained to recognize only single presses can make reasonable predictions of multi-press deformations and damage states, while simultaneously monitoring the environment's temperature and humidity (*49*). However, existing approaches have been limited to simple skin shapes because of the challenges involved in using standard EIT devices for complex 3D shapes (*50*); even shell structures, which are topologically equivalent to circular 2D skins, will produce weaker responses to a given stimulus due to the increased length of their current paths. Zhang and Harrison used 28 configurations of electrodes placed around a human's wrist to differentiate between hand gestures using machine learning (*51*): while this demonstrated the promising potential of EIT measurements to reconstruct more complex shapes, multimodal stimuli were not considered.

In this work, we aim to develop tactile skin technologies that can be seamlessly integrated into existing robotic devices while providing high-density multimodal tactile information. To do so, we explore the information structuring of high-density EIT on complex-shaped single layer sensorized membranes which respond to multimodal tactile cues. Using EIT hardware, we select electrode combinations which generate specific electric fields across a healable hydrogel, developed for soft strain-sensing applications (*52*). The hydrogel's thermoreversibility allows it to be cast into sensorized 3D skins, and we demonstrate our multimodal sensing approach on a full-size hollow hand with electrodes positioned only around its wrist.

We use our approach to balance between the 1.7 million available information channels and a bandwidth of up to 33 kHz, by identifying and only monitoring the setup-specific channels providing information most efficiently. In doing so, we demonstrate how the hand can predict environmental temperature and humidity, localize light touches to 25 mm over

a 38,000 $mm^2$ area, and provide proprioceptive data when its fingers are actuated.

Figure 1a presents an overview of our framework for multimodal sensing. A soft sensorized membrane functions as the skin, cast from a gelatin-based hydrogel. This hydrogel, presented in (*52*), is low-cost, stretchable, piezoresistively responds to strain, and can be used to monitor environmental temperatures and humidities. Its electrical and mechanical properties can be tuned through its composition, enabling application-specific designs. Here, we depict the skin as a circle, but its single layer thermoreversibility means it can be straightforwardly cast into more complex morphologies, such as a hollow human hand.

To monitor the skin's multimodal interactions, up to 32 electrodes are arranged around its perimeter. Multiple tetrapolar electrode excitation patterns can be quickly swept across these electrodes using EIT electronics: two electrodes inject an AC current to generate an electric field across the membrane, and the resulting voltage difference is measured between two other electrodes. Through various mechanisms, multimodal stimuli cause changes in the electric field, which are recorded by the peripheral electrodes. By carefully selecting the electrode configurations which we use to monitor the skin, the system's output information can be structured to efficiently return modality and application-specific data. We select these configurations directly from physical measurements, ensuring that our approach can be directly applied to complex physical setups without requiring simulations.

In an idealized system, many of the available configurations are linearly dependent. Instead of assuming our system to be ideal, we consider the signals returned by all possible configurations, ensuring that information is not lost due to small nonlinearities in the electronic circuitry and physical coupling. This approach means that the four electrodes used for each measurement are chosen completely independently, giving 863,040

($= 32 \times 31 \times 30 \times 29$) possible configurations of 32 electrodes. By measuring the amplitude (as root mean square: RMS) and phase shift of all alternating current (AC) signals, 1,726,080 information channels are available for data-driven evaluation. At its highest speed, our circuitry can monitor all of these channels at a 0.02 Hz frame rate. By selectively structuring our excitation configurations, this frame rate can be linearly improved to a maximum of 33 kHz (when monitoring 1 configuration), while providing sufficient information about the form and location of the multimodal stimuli. Using our sensor-specific methodology we envisage a pipeline for multimodal skin calibration: all available channels are first monitored during a small range of physical tests, which are then used to select a subset of configurations to best strike the balance between speed and information content while accounting for noise, setup imperfections, nonlinearities, and signal redundancies. Unlike existing cutting-edge works (*31, 47, 48*), our surfaces can be cast into complex 3D shapes, and can respond to multimodal stimuli using only a single-layer structure. We move beyond previous 3D shape sensorisation demonstrations – such as humanoid faces (*32*) – by explicitly considering multimodality, incorporating responses from over 1000 tactile stimuli and 100 hours of environmental monitoring.

We first develop our approach and analyze the material-level responses using an eight-electrode circular membrane of the gelatin-based hydrogel, before applying the pipeline to a complex-shaped soft single-layer hand, where we demonstrate its multimodal capabilities.

# Results

## Multimodality through material-level stimuli response

Figure 1b depicts the membrane on which we first tested our information structuring approaches. A 10 cm diameter hydrogel circle was surrounded by eight electrodes, provid-

ing 1680 potential tetrapolar configurations and 3360 potential information channels. All could be monitored by the high-speed electronics at up to 9.8 Hz (Table S1) — we selected a 1 Hz rate to minimize the noise present in the generated electric field measurements. By taking four-electrode measurements, we ensured that many channels were available for our data-driven analyses (1680 configurations compared to 56 for two-electrode measurements), as well as lessening the effect of contact impedances on our measurements.

We examined how six types of active stimuli affect the membrane's electric field: pressing with an insulated probe, touching with a human fingertip in one or multiple locations, touching with a conductive object, damage, and localized melting. Each of these stimuli is depicted in Figure 2a, above their expected detection mechanisms. A seventh stimulus - lightly touching with an insulated (plastic) object - was included as a baseline, since this was not expected to change the generated electric field. Figure 2b plots the idealized simulations of the stimuli's effects on one of the circular skin's electric fields (see *Simulations* in *Materials and Methods*). Electric current streamlines are plotted in grey, and the induced voltage equipotentials are plotted in orange.

Straining the hydrogel with an insulated press or cutting it with a scalpel both acted to locally decrease its conductivity, causing less current to flow through the stimulated region. For Figure 2b's electrode configuration and stimulus location, the simulation predicts that this leads to an increase in the measured voltage (more equipotentials terminate between the measurement electrodes) which was also observed in the real data. Since damaging the membrane locally reduces its conductivity to zero, this had the largest magnitude (28 mV), whereas the response to the insulated press was only 2.2 mV. This was more than the insulated touch baseline in Figure 2b's final column: as expected, this difference was negligible. Though both stimuli locally decreased the membrane's conductivity, differences in their spatial distributions could be identified by data-driven methods

for modality classification: damage cases will demonstrate very sharp transitions between conductivities, whereas a single press will cause a more gradual transition, resembling a 2D Gaussian curve. Instead of inferring these distributions from a reconstructed conductivity map, we looked for approaches in which such differences are identified directly, facilitating our method's scalability to more complex 3D skins.

Similarly, the melting and conductive touch modalities both caused a local increase in conductivity, which the simulation predicts will result in a decrease in the measured voltage. In our physical experiments, decreases of 19 mV and 26 mV were measured respectively, suggesting that the high conductivity of the steel bolt had the greatest effect. As before, we expect the different spatial distributions of these conductivity changes to be directly recognizable by an empirical approach. In addition, the two modalities behaved very differently temporally, which could be exploited by recurrent neural networks to provide additional information.

Finally, the effect of human touch was considered, which we split into two cases: single finger touches and multi-finger touches. As described by Zhang et al. (*33*), single-finger touches draw a small amount of current to ground via the shunting effect, which cannot be represented with standard EIT models. Rather than modelling a current sink, Figure 2b approximately modeled this as a local decrease in conductivity: a positive voltage change was observed, though its magnitude was difficult to predict. Conversely, touching the membrane with two fingers of the same hand provided a viable new path for the current to flow, since human skin has a comparable resistance to the hydrogel (*52*). Again, this was not straightforwardly simulated; Figure 2b's attempted local conductivity increase predicted little change in the measured voltage, rather than the substantial decrease observed.

## Decoupling multimodal information

So far, Figure 2b has considered only the RMS response of one of the 1680 available electrode configurations. For each configuration, the measured signal's magnitude and phase shift could both be measured, giving a potential information throughput of 3360 information channels per frame. The information redundancies which these channels contain can be used to uniquely identify, localize, and transfer knowledge between various modalities without the need for stimuli-specific devices. In a fully implemented system, different configuration subsets would then be monitored based on the desired stimuli, information rate, and required precision.

Some typical responses of the 3360 channels are shown in Figure 2c. Each row plots the normalized 10 kHz signal against time from one of these channels as a finger was touched to three discrete locations on the physical membrane, and removed between trials. Responses were visible in both the magnitude (RMS) and phase information channels. Importantly, the overall response was noticeably different for each of the three locations: using suitable information processing, localization is possible. The RMS and phase responses look very different for different modalities: Figure 2c also plots the raw responses of the 3360 channels during localized melting of the same 3 locations. Rather than discrete events, melting was characterized by sharp steps when heat is applied, followed by a cooldown period in which responses begin to drift back towards their starting point. These time-dependent behaviors are shown for two selected configurations at the right-hand side of Figure 2c. At this stage, we do not know which configurations are best for predicting the type and location of each stimulus; we next explore how these measured responses can provide insights into the key similarities and differences between the modalities. Unless otherwise specified, tests were performed at 10 kHz. Figure S1 justifies the frequency selection, comparing the localized melting responses at three frequencies.

For the 8-electrode EIT skin, we can devise data-driven methods to select the information channels that provide maximum information about the tactile cues (See supplementary methods S4 for a simulation study on noise-free data for the same problem). Figure 3 considered three objectives in data-driven configuration selection: finding those which return the best information for each modality, those which return the best information regardless of modality, and those which are best for distinguishing between modalities. To do so, we individually applied 7 modalities to the circular membrane: in addition to Figure 2's modalities, we also applied presses with a human finger, which we consider as the combination of touch and insulated pressing mechanisms. Three arbitrarily-chosen locations were used, marked A→C in Figure 3a. The 1680 electrode configurations were recorded as all seven combinations of A, B, and C were applied, and their channel information was ranked using principal component analysis (PCA) to determine which most strongly influenced the variability of the response (see *Types of Stimuli* in *Materials and Methods*. Additional insulated-press experiments with six fixed locations were repeated in Figure S13). As depicted in Figure 3b, each modality's PCA ranking was used to construct a characteristic 'fingerprint' which we used as the basis of our configuration selection approach. The fingerprints are arranged such that each single row represents a fixed driving electrode pair, meaning that regular structures appear in the data - based on the differences between the fingerprints, we visually gain an idea of their most important configurations. In the fingerprints, each modality's best configurations are represented by the darkest pixels: the top-ranked configuration for each is shown in Figure 3c. The insulated touch was the only fingerprint in which regular structures do not appear, since the skin cannot respond to this modality. Hence, the insulated touch modality was not analyzed further. Human press, which combines the human touch and press modalities, appeared to be dominated by the human touch mechanism, with very similar fingerprint

structures and the same top-ranked configuration.

To determine the best configurations regardless of modality, five of the fingerprints were averaged, giving the blue general fingerprint of Figure 3c, in which darker pixels indicate better configurations. Given the similarities of the human press and human touch modalities, only human touch was used to construct this fingerprint to avoid skewing of the result. The top four general configurations are shown, which provide the maximum information content about the stimuli.

Finally, to identify unique configurations - those which respond in one modality more than the others - we considered the difference between the modality's own fingerprint and the general fingerprint. This approach is illustrated for a human touch in Figure 3c: the darkest pixel of the green fingerprint represents its unique configuration, which was different to any of those already identified. This uniqueness was true for all configurations identified in Figure 3c, representing the information channels, which could be used to identify particular modalities. From these identified channels, we can immediately see why a data-driven approach is most beneficial for decoupling multimodal signals, using high-density EIT to generate information.

The benefits of our fingerprinting approach are demonstrated in Figure 3d, where the top-ranked general configuration (G1) was used to measure the responses of five modalities at the three locations. As expected, the insulated touch did not respond beyond experimental noise, whereas all others had responses which vary with location. The differences in magnitude between modalities is an indicator of how difficult each will be to analyze: insulated presses gave a much weaker response than human or conductive touches. Response weakness could be partially addressed using the unique configurations: the final plot of Figure 3d shows how the average response at the three locations was changed from G1 by the unique configurations of four modalities. In three of the four

cases, our fingerprinting approach identified configurations which maximized the signal from their particular modality. Only human press - which was not used in the general fingerprint - did not achieve this, instead maximizing the human touch change. This suggests that, although it will be difficult to distinguish between the two modalities, any localization results from one could be straightforwardly transferred to the other due to their similar mechanisms. Transferring knowledge between the modalities with different mechanisms is more of a challenge: we considered an extension of our data-driven approach in Figure 4.

## Estimating multimodal information

To understand how we could differentiate between multiple stimuli, we first examined the similarity among all modality responses during Figure 3b's seven experiments, based on the coefficients of the first principal component (see supplementary methods S1). The results are plotted in Figure 4a, where thicker connections indicate a higher similarity metric. As well as being similar to each other, both human modalities were very similar to the modalities which locally increase conductivity: conductive touch and melting. Conversely, both had minimal similarities to damage and insulated pressing, which locally decreased conductivity. We aimed to identify a modality which is sufficiently similar to all others, such that its further analysis provided insights into all modalities. Conductive touch was selected for this purpose; we first learned to localize the touch and then examined how this knowledge can be transferred: Figure 4b.

For localization, Figure 4c is based on the responses of the 3360 information channels to 1000 random placements of a steel nut onto the membrane by a robotic arm (Video S1). The information from the 3360 channels could be utilized to estimate the bolt's location using standard regression algorithms.

Rather than using all channels as the input to a feedforward neural network, we used only the $N$ best configurations, after all 1680 configurations were ranked using one of three methods. In an ideal system with no noise or nonlinearities, localization of a single stimulus could be performed with just five information channels (Figure S11). Since our physical system did not behave ideally, this ranking approach was used to ensure measurement efficiency for complex setups, and could be straightforwardly expanded to non-circular membranes and skins. Two of the three ranking methods did not use any ground truth position data: 'PCA' was the same ranking used to build Figure 3's fingerprints, and 'Environment' performed its ranking based on how well the channels correlated to changes in humidity of the membrane over an 62-hour period (Figure S2). The final ranking method used the position data as the basis of a statistical F-Test (supplementary methods S1). All were compared to 'Adj/Opp', which tested opposite and adjacent electrode positions (Figure S3). These electrode configurations were selected as a comparison due to their widespread usage and practicality in sensorized robotic skins (*32, 34–36*); we note that, in more traditional EIT setups, more suitable configuration approaches have been identified for the reconstruction of conductivity maps (*53*).

When the localization errors of a 10% test set were examined ($N = 1 \rightarrow 150$) in Figure 4c, all three ranking methods performed better than the adjacent/opposite configurations, with the F-test ranking quickly converging to errors less than 10 mm. The improvement of the data-driven rankings stemmed in part from their ability to exploit asymmetries and nonlinearities in the physical material composition, multiplexer performance, and contact impedances (Figure S4). The distributions of errors over the membrane using the 20 best configurations are shown: although PCA gave some regions of good localization, the adj/opp ranking had high errors distributed across the entire membrane. F-Test gave a near-uniform distribution of low errors across the membrane's surface.

The F-Test ranking method provided a successful way of efficiently structuring the skin's output data, with its top 50 configurations resulting in better localization than 150 configurations of a standard sweep. We next used these top 50 configurations to map unseen modalities into a 2D plane where different stimuli could be visualized, built from the conductive touch data's first two principal components: Figure 4d.

When the F-Test mapping was applied to the seven experiments of conductive touch, clusters were visible, corresponding to the untouched state, each individual location, and each multi-location combination. Using the vectors between each stimulus and the untouched state in Figure 4d, each multi-location event could be reasonably predicted by superposing its individual locations (Figure S5). This observation suggests that each location elicits relatively independent responses from the structured channels - a behavior which we encouraged by statistically ranking the channels. Through finding configurations which identify specific regions of the membrane, we expected our structured output data to be generalizable to new modalities, which we tested in Figures 4e-g. These figures used the same mapping, built from conductive touch's responses, to visualize the responses of three different modalities at the same locations: insulated press, human press, and melting. The scale was kept consistent: larger vector magnitudes were due to greater raw responses. We have already seen in Figure 3d that insulated presses have the smallest magnitude, but we now look at the direction of its vectors (Figure 4e), which were all in opposite directions to those of conductive touch (as shown directly in Figure S5). This shift in direction occured because the pressing caused a local decrease in conductivity, unlike conductive touch's local increase - knowing this mechanism, we could use the mapping to predict locations of the unseen modality, for both single and multi-press events - superposition also applies to this new modality. Further multi-press predictions of up to six simultaneous insulated presses were explored in Figure S13, where this superposition

was exploited by considering each location independently.

When mapping human press stimuli (Figure 4f), there was a difference between single and multi-press modalities, as predicted by Figure 2a's different mechanisms. The single-touch vectors of A, B and C (corresponding to the locations marked in Figure 3a) were in very similar directions to that of conductive touch. However, multi-press produced a new path along which the current can flow, and superposition did not apply - multi-press produced much greater responses. Multi-press events were still distinguishable, being separately clustered in the 2D mapping, but additional modelling layers would be required in order to accurately predict their locations.

The inverse relation between insulated press and conductive touch response vectors implies that melting, which locally increases conductivity, should result in response vectors aligning with those of conductive touch. This was the case: Figure 4g shows a parametric plot with time as the membrane was heated and allowed to cool at A, B and C, each of which caused an outward motion in the same direction as that of the conductive touch (Video S1). These transferability findings (illustrated fully in Figure S5) indicate that, by knowing the mechanism by which a sensing modality affects the electric field of an asymmetric membrane, the results from training on only one modality can be used to make sensible predictions and the locations of totally unseen modalities. Coupled with knowledge of the unique configurations (Figure 3c), this transferability provides a data-driven pipeline for multimodal sensing in the skin: unique configurations are monitored to detect and classify a particular stimulus, the location of which is then predicted using conductive touch's trained model. In addition, we know from Hardman et al. (*52*) that environmental conditions can be straightforwardly monitored using just a handful of configurations, facilitating a skin which responds not only to multiple stimuli, but can also track the conditions in which it is doing so. The data-driven nature of our approach

means that it could be applied to setups for which analytic approaches would ordinarily struggle: 3D skins and anisotropic conductivities.

## A single layer sensorized soft hand

To demonstrate how combining information structuring with high-density EIT can enable high functional robotic skins, we moved from the 2D circular membrane to a more complex 3D morphology: a full-size hollow 3D hand cast entirely from the soft sensorized hydrogel. Figure 5 presents the key components of its design - with 32 electrodes arranged around its wrist, there were 863,040 available electrode configurations and 1,726,080 available information channels. These configurations were used to generate electric fields across the hand, the monitoring of which enabled multimodal sensing through the mechanisms introduced in Figure 2. Despite the complex 3D shape, information-rich subsets of the 863,040 electrode configurations could be identified with our approach, such that stimuli could be recognised and interpreted with an efficient balance of information rate and content.

A new proprioceptive response was also introduced: strains from the bending of the fingers caused conductivity changes which could be detected in the raw signals. Unlike previous skins for robotic hands, the entire surface area of our design contained no soft/rigid interfaces, since electrodes were introduced only at the wrist. The free surface made the skin fully stretchable, fully continuous, and free to capture multimodal interactions occurring anywhere over its surface. As the hand was made from just one material, there was no risk of delamination. Local damage to the surface does not affect device architecture and the material itself exhibits healing properties (*52*), making the artificial skin highly robust.

Figure 5b depicts the hand's fabrication process: a silicone mold was cast around a 3D-

printed positive, before a smaller 'inner positive' was inserted, a flexible sleeve containing conductive threads was added, and the hydrogel was cast. After removal from the mold, the inner positive was removed through the empty cross section of the wrist to leave a soft hollow membrane, which was firmly secured into a base through which the 32 electrodes were wired. More details can be found in Figure S7, and in the supplementary methods S3.

The hand immediately responded to human touch, conductive touch, and finger bending (Figures S8-S10). We focus here on the information structuring that is required for human-robot interactivity (localizing light human touches over the skin's surface) and for environmental monitoring (of temperature and humidity). Given the electrode positions, any generated electric fields will be weakest at the skin's fingertips. To account for this distribution, our data-driven ranking approach will skew towards selecting configurations which provide localization information towards these areas, rather than only near the base. Alternatively, the hydrogel's composition could be locally varied to provide material-level information structuring, increasing the conductivity of channels which encourage current flow towards the fingertips (*36*). This approach was briefly explored in Figure S6.

In Figure 6, we demonstrate how our data-driven ranking methods can perform human touch detection on this complex 3D surface. Firstly, all 1,726,080 channels were monitored as the hand was touched in three locations (Figure 6a). Even touches at the fingertip, furthest from the electrodes, could be seen in the raw data. From these representative responses, Figure 3's approach was used to generate a $780 \times 992$ fingerprint, from which the 2784 best-ranked configurations were selected.

To characterize our method's localization capabilities, 1080 random locations over the hand's 38,000 $mm^2$ area were touched while 11,136 channels were monitored: the 2784 selected fingerprinting configurations, and the 2784 adjacent/opposite EIT configu-

rations. By pre-filtering 5568 of the 863,040 available configurations, we balanced between a dataset which could be collected efficiently (11,136 channels every 6.5 s - Table S1), and collecting sufficiently structured data to run a more thorough ranking for successful localization. Before any further channel reduction was done, the method of weighted activation maps (WAMs, presented in (*49*)) was used to predict the locations of a 10% test set, given $N$ channels. Figure 6b plots the resulting localization errors ('without ranking'), which converged very slowly, with localization errors averaging more than 40 mm even when using 500 random channels. However, when the F-Test ranking method was introduced to structure the standard configurations, localization errors fell below 30 mm using just 40 channels, as our data-driven search identified those which were capable of providing the most beneficial information despite the presence of measurement noise (Figure S12).

With more configurations available to structure, the localization became even more accurate and efficient: Figure 6b's rightmost graph plots the $N = 500$ localization errors. Using F-Test ranking, localization was possible to 24.7 mm over the 380 $cm^2$ area of the hand (Video S2). To examine how this was achieved, Figure 6b also demonstrates the activation maps of the 10 best configurations: their average responses to 1080 touches over the area of the hand. Using only these 10 signals, localization errors below 40 mm could be achieved. In each, a particular area of the hand responded most strongly to the light touches: by combining multiple such configurations, the WAMs method could efficiently predict the touch location. Localizing the touch with so few channels enabled higher frame rates during data collection (up to 3.3 kHz for 10 channels in Table S1), promising the analysis of increasingly dynamic data. Additionally, this localization of human touch was achieved with fewer than 496 channels - the maximum number of independent channels predicted by N-port theory (*46*) - ensuring that additional information is available for multimodal predictions.

For example, the soft 3D hand could also monitor and predict its environmental conditions, as shown in Figure 6c and Video S2. Here, the responses of the 5568 configurations were recorded over a 100-hour period in the laboratory. During this time, the environmental temperature and humidity moves between $19 \leftrightarrow 25$ °C and $38 \leftrightarrow 72$ % respectively. By ranking the responses using Figure 4's F-Test approach, 50 signals were sufficient to train a neural network to accurately predict environmental temperature and humidity in a 10% test set, as shown in Figure 6c. These fluctuations caused changes in the hydrogel's conductivity, which affected the measurements of the skin's generated field. Subsequently, a global drift could be seen: Figure 6a plots the mean RMS response of all 863,040 configurations, averaged over 870 groups of 992 channels. Though some channels were noisier than others, this drift corresponds to ground truth measurements of the actual environmental conditions. Additionally, tactile data could be recorded and predicted during this same period: the gray bars indicate a period over which 250 random locations were touched, and localized with an average error of 26.3 mm. Figure 6d shows the distribution of localization errors: the structured configurations kept this low over the majority of the hand, with higher errors mostly at the fingertips. In Figure 6e, the WAMs predictions of eight consecutive test set touches are plotted, where brighter yellow regions are those predicted most likely to contain the stimulus. With an average error of 25.1 mm, these provide a representation of typical predictions over the 1,080 recorded touches. In three cases, the front/back classification was predicted incorrectly. These were cases in which the stimulus was very close to the perimeter, such that the front and back touches were physically very close. More examples are shown in Video S2. Additionally, an initial application of our channel-ranking + WAMs approach to further multimodal predictions is presented in Figure S14. Human multi-touch predictions across a new 32-electrode 3D hand were made at the same time as local temperature predictions at the base of its

thumb. Channel-ranking was used to treat front predictions, back predictions, and temperature predictions independently. Results are shown further in Figure S15 and Video S3, while full details are given in supplementary methods S5.

# Discussion

Current multimodal tactile sensing technologies are developed from a bottom-up approach, designing modality-specific devices which are combined using complex fabrication techniques and smart materials to make them flexible and scalable. This approach makes them difficult to manufacture, expensive, prone to delamination and damage, and susceptible to interference. Our results demonstrate a top-down approach for the multimodal sensorization of complex skins: using our information-structuring framework, we are able to localize light touches over the surface of a homogeneous hand with electrodes positioned only around its wrist. Thirty two electrodes provide more than 1.7 million information channels across the sensorized material, containing data from multimodal interactions and environmental conditions with inbuilt redundancies which ensure robustness. This abundance of data presents challenges in the processing of sensory information that stimuli-specific sensing devices do not have, but our architecture provides more flexibility in the design, fabrication, and scale. To address the challenge of efficiently obtaining relevant state information from these numerous channels, we present a multilevel information structuring method. Using passive information from the environment with the combination of statistical techniques, modality-relevant information channels can be quickly identified. This is followed by standard nonlinear regression for state estimation. We demonstrate how the information structuring of such channels can be used to identify and process multimodal stimuli, increase the efficiency of tactile localization, and transfer knowledge between modalities. Using this approach, we highlight a promising

route for increasing the complexity of 3D multimodal skins with peripheral electrodes for direct application to wearable sensors, robots, and prosthetic devices.

So far, we have demonstrated our sensing strategy using a homogeneous material, showing the benefits of our information structuring approach to the multimodal sensing of complex shapes. Even with F-Test ranking, the homogeneous material properties led to decreased sensitivities at the hand's fingertips, furthest from the electrodes. As EIT technologies continue to be developed for single layer 3D shapes, sensitivity distributions can be influenced in two ways: electrode repositioning, and material anisotropies. Repositioning electrodes to locations where they will generate stronger signals makes the areas more sensitive, but at the expense of restricting motions, physical interactions, and increasing delamination risk. Conversely, the introduction of conductivity anisotropies (as explored in Figure S6) into the material would serve to bias the direction of current flow while keeping electrodes at convenient locations. With hydrogels, this could be implemented through local changes in composition; a skin's initial conductivity distribution and electrode location could be optimized in simulation before fabrication. Still, without first principle models, it is not possible to predict the properties of our sensory skin. This makes specification-driven design and design optimization challenging. Data-driven design optimization techniques have to be employed in this case (*54, 55*), and we expect that a realistic design pipeline of our approach would couple the faster iterations of simulated models with the empirical data of physical modelling.

Figure 1 introduced the hydrogel composition used as the basis of the sensorized membranes throughout this work. Its responsiveness to particular stimuli determined the range of multimodal properties which we were able to demonstrate; those capable of influencing a generated electric field can be monitored through our approach. Similarly, the selection of different conductive and functional materials could be used to introduce new modalities

including magnetic, chemical, and light sensitivities. For a material's complete system integration, these electrical properties must be considered alongside its mechanical, fabrication, and robustness characteristics. Hydrogels are typically associated with 'drying out' over short time periods: though the composition used here can remain stable over multiple months (*52*), its mechanical properties and physical dimensions fluctuate within a typical range of environmental temperatures and humidities, and it has a relatively low maximum operating temperature. The effects of humidity can be lessened through the introduction of a non-permeable covering, though this moves into a multi-layer system in which the chances of delamination and adhesion issues are greatly increased. Instead, for more stable implementations conductive elastomers - such as the carbon-infused silicones popular in soft robotic systems - could be explored.

By using a single layer skin, our hand was stretchable and could not delaminate. Its weakest points were at the only remaining soft-rigid connections: the wrist. As described in the supplementary text, clamped connections, conductive thread, and adhesives of intermediary stiffness were used to ensure this interface was as robust as possible. Subsequent iterations and improvements in flexible electronic adhesion could look to integrate more flexibility into these connection points, transforming them into safer soft-soft interfaces.

Additional future work includes the exploration of methods for the transferability of learned channel rankings between different sensors. We began our approach by neglecting reciprocity assumptions within the system in favour of a data-driven approach: once any hardware nonlinearities have been learned then this step may not be necessary, improving training efficiency. Once efficient frameworks have been developed, a promising direction of development is the execution of high-level touch-driven tasks for robotic manipulation using sensorized skin. Since the soft skin is hollow and stretchable, we can easily wrap

existing robotic manipulators with minimal effects on the robot's motion. Raw data from the EIT channels after the first stage of information structuring or fully processed multimodal information can be used as state observations to close the loop for contact-rich tasks (*56*).

# Materials and Methods

## Electrically Conductive Membrane

The electrically conductive skin was cast from a gelatin-based hydrogel, as described by Hardman et al. (*52*). Gelatin powder (MM Ingredients) was mixed with water, glycerol (Fisher Scientific) and citric acid monohydrate (Fisher Scientific) at a mass ratio of 1:1.5:1.5:0.2, and left to homogenize for 48 hours in an oven at 50°C, during which salt (Sainsburys) was added at a mass ratio of 1:0.1 to the gelatin powder. To create the circular membrane from Figures 1→4, this mixture was poured into a laser cut acrylic mould of 110 mm diameter and 3 mm thickness. Once solidified, the membrane was clamped between two laser cut acrylic frames, pressing 8 equally stainless steel M2.5 bolts into its surface at a 100 mm diameter to function as the electrodes. This setup was bolted onto a 3D-printed support, which held a 90 mm cylinder of Ecoflex 00-20 silicone underneath the exposed hydrogel surface. The resulting setup is shown in Figure 3a: any presses of the skin also pressed into the silicone substrate. Figure 1 shows the interface between the electrodes and the high-speed electronics: one crocodile clip was clamped to each of the eight electrodes, which joined to a 32-pin ribbon cable via an IDC breakout board. Figures 3 and 4's experiments were performed at environmental conditions of 55% humidity and 19°C. Full details of the hollow hand's casting process and electrode integration are provided in the supplementary methods S3, and CAD files provided in the code repository.

## Electronics

Throughout this work, electric fields were generated and measured using Zhu et al.'s open source *EIT-kit* motherboard (shown in Figure 1b), designed for human health and motion monitoring via electrical impedance tomography (*57*). To match the impedance of the hydrogel, four resistor values were changed from the original design: R7, R8, R21 and R22 were set to either 100 Ω (2D membrane) or 50 Ω (3D hand). The Teensy 4.0 microcontroller on which this runs was programmed through the Arduino IDE, and measurements were returned to a serially-connected laptop through a USB cable. Voltage and current gains were set manually for each setup, as were each configuration's electrode locations via its multiplexer. Table S1 details the frequencies and speeds used throughout this work: the fields from injection frequencies between 10 and 100 kHz were measured using the onboard 20 MHz ADC. By varying the controller's averaging factor and wait times, single measurements were returned at a rate of up to 33 kHz. Specific rates were selected for each experiment to compromise between measurement speed and noise reduction.

## Simulations

Figure 2b and c's electric field simulations were generated using EIDORS's inbuilt forward solver (*58*), implemented in MATLAB 2023a. A circular model with 8 electrodes and low vertex density was constructed, with identification string `d2d1c`. Stimulation patterns were input manually, and the field visualized using MATLAB's `streamline()` and `contour()` functions for current and voltage, respectively. To simulate the insulated touch's effect, a homogeneous membrane was assumed, whereas other modalities were represented by changing the conductivity of a circle one fifth the diameter of the membrane. The 'new path' mechanism was represented using a variable-conductivity ellipse.

In Figure 2b, current was injected at electrodes 5 and 8 while being measured at electrodes 2 and 4. This corresponds to configuration 1598, which was selected such that stimuli at point A resulted in a visible effect to the generated field. In configurations 352 and 902, this order was [2, 6, 3, 7] and [3, 5, 1, 4] respectively. Code is provided with this manuscript.

## Types of Stimuli

Figure 3's control stimulus - insulated touch - was applied by placing 1.5 g polypropylene twist caps at locations A, B, C, A + B, A + C, B + C and A + B + C in turn for one minute, with one minute gaps between each stimulus. Insulated press, conductive touch, human touch and human press followed the same order and timings (photos of each are given in Figure 3a), with conductive touch using a 6.5 g stainless steel bolt, human touch using the fingers of the experimenter's left hand to gently contact the membrane, human press using the fingers of the experimenter's left hand to depress the membrane by approximately 10 mm, and insulated press using 5 mm diameter PLA probes attached to a UR5 robotic arm to depress the membrane by 8 mm. For the melting stimuli, a rework station's heat gun, set to 200°C, was brought close to locations A, B and C in turn, each for 15 seconds with 5 minute intervals for cooling. During damage, the experimenter wore nitrile gloves and used a 10A scalpel blade to cut the membrane at locations A, B and C, holding each cut open for 1 minute then releasing for one minute before cutting the next. During all modalities, RMS and phase information from all 1680 channels at 10, 50 and 100 kHz were monitored at a frame rate of 0.33 Hz (Table S1). The 10 kHz recordings were used in subsequent analysis.

### Processing and Localization

Information processing and stimulus localizations were implemented using MATLAB 2023a. Supplementary methods S1 provides specific details behind the creation of Figures 3b→d and 4a→c, 4e→g. Supplementary methods S2 provides specific details behind the localization methods of Figures 4d and 6a→e.

### Statistical analysis

Figures 2, 3, 4 and 6 present data from individual experiments, using a large number of channels and randomized locations, which are reported in the captions. Reported localization errors throughout the manuscript are the mean errors of an isolated test set (10% unless otherwise stated). Details of specific implementations are provided in the supplementary methods, and in the attached code.

## Supplementary materials

- Supplementary Tables S1 to S2
- Supplementary Figures S1 to S15
- Supplementary Methods S1 to S5
- Supplementary Videos S1 to S3

## References

1. R. S. Johansson and J. R. Flanagan, "Coding and use of tactile signals from the fingertips in object manipulation tasks," *Nature reviews. Neuroscience*, vol. 10, no. 5, pp. 345–359, 2009.

2. R. S. Dahiya, *Robotic tactile sensing technologies and system / Ravinder S. Dahiya, Maurizio Valle.* Dordrecht: Springer, 2013.

3. J. A. Rogers, T. Someya, and Y. Huang, "Materials and mechanics for stretchable electronics," vol. 327, no. 5973, pp. 1603–1607, 2010.

4. B. Shih, D. Shah, J. Li, T. G. Thuruthel, Y.-L. Park, F. Iida, Z. Bao, R. Kramer-Bottiglio, and M. T. Tolley, "Electronic skins and machine learning for intelligent soft robots," *Science Robotics*, vol. 5, no. 41, p. eaaz9239, 2020.

5. S. Zhang, Z. Chen, Y. Gao, W. Wan, J. Shan, H. Xue, F. Sun, Y. Yang, and B. Fang, "Hardware technology of vision-based tactile sensor: A review," *IEEE Sensors Journal*, vol. 22, no. 22, pp. 21410–21427, 2022.

6. Y.-L. Park, B.-R. Chen, and R. J. Wood, "Design and fabrication of soft artificial skin using embedded microchannels and liquid conductors," *IEEE Sensors Journal*, vol. 12, no. 8, pp. 2711–2718, 2012.

7. O. Shorthose, A. Albini, L. He, and P. Maiolino, "Design of a 3d-printed soft robotic hand with integrated distributed tactile sensing," *IEEE Robotics and Automation Letters*, vol. 7, no. 2, pp. 3945–3952, 2022.

8. K. Gilday, T. George-Thuruthel, and F. Iida, "Predictive learning of error recovery with a sensorized passivity-based soft anthropomorphic hand," *Advanced Intelligent Systems*, vol. 5, no. 7, p. 2200390, 2023.

9. Y.-L. Park, C. Majidi, R. Kramer, P. Bérard, and R. J. Wood, "Hyperelastic pressure sensing with a liquid-embedded elastomer," *Journal of Micromechanics and Microengineering*, vol. 20, p. 125029, nov 2010.

10. S. Russo, T. Ranzani, H. Liu, S. Nefti-Meziani, K. Althoefer, and A. Menciassi, "Soft and stretchable sensor using biocompatible electrodes and liquid for medical applications," *Soft Robotics*, vol. 2, no. 4, pp. 146–154, 2015.

11. H. Yousef, M. Boukallel, and K. Althoefer, "Tactile sensing for dexterous in-hand manipulation in robotics—a review," *Sensors and Actuators A: Physical*, vol. 167, no. 2, pp. 171–187, 2011. Solid-State Sensors, Actuators and Microsystems Workshop.

12. J. Tu, M. Wang, W. Li, J. Su, Y. Li, Z. Lv, H. Li, X. Feng, and X. Chen, "Electronic skins with multimodal sensing and perception," *Soft Science*, vol. 3, no. 3, 2023.

13. Z. Yuan, S.-T. Han, W. Gao, and C. Pan, "Flexible and stretchable strategies for electronic skins: materials, structure, and integration," *ACS Applied Electronic Materials*, vol. 4, no. 1, pp. 1–26, 2021.

14. M. Weigel, T. Lu, G. Bailly, A. Oulasvirta, C. Majidi, and J. Steimle, "iskin: Flexible, stretchable and visually customizable on-body touch sensors for mobile computing," in *Proceedings of the 33rd Annual ACM Conference on Human Factors in Computing Systems*, CHI '15, (New York, NY, USA), p. 2991–3000, Association for Computing Machinery, 2015.

15. M. Teyssier, G. Bailly, C. Pelachaud, E. Lecolinet, A. Conn, and A. Roudaut, "Skin-on interfaces: A bio-driven approach for artificial skin design to cover interactive devices," in *Proceedings of the 32nd Annual ACM Symposium on User Interface Software and Technology*, UIST '19, (New York, NY, USA), p. 307–322, Association for Computing Machinery, 2019.

16. S. Harada, W. Honda, T. Arie, S. Akita, and K. Takei, "Fully printed, highly sensitive multifunctional artificial electronic whisker arrays integrated with strain and temperature sensors," *ACS nano*, vol. 8, no. 4, pp. 3921–3927, 2014.

17. Y. Wang, D. Liu, Y. Zhang, L. Fan, Q. Ren, S. Ma, and M. Zhang, "Stretchable temperature-responsive multimodal neuromorphic electronic skin with spontaneous synaptic plasticity recovery," *ACS nano*, vol. 16, no. 5, pp. 8283–8293, 2022.

18. J. W. Booth, D. Shah, J. C. Case, E. L. White, M. C. Yuen, O. Cyr-Choiniere, and R. Kramer-Bottiglio, "Omniskins: Robotic skins that turn inanimate objects into multifunctional robots," *Science robotics*, vol. 3, no. 22, 2018.

19. T. Mukai, M. Onishi, T. Odashima, S. Hirano, and Z. Luo, "Development of the tactile sensor system of a human-interactive robot "ri-man"," *IEEE Transactions on Robotics*, vol. 24, no. 2, pp. 505–512, 2008.

20. A. Schmitz, M. Maggiali, L. Natale, B. Bonino, and G. Metta, "A tactile sensor for the fingertips of the humanoid robot icub," in *2010 IEEE/RSJ International Conference on Intelligent Robots and Systems*, pp. 2212–2217, 2010.

21. T. Yoshikai, H. Fukushima, M. Hayashi, and M. Inaba, "Development of soft stretchable knit sensor for humanoids' whole-body tactile sensibility," in *2009 9th IEEE-RAS International Conference on Humanoid Robots*, pp. 624–631, 2009.

22. P. Mittendorfer and G. Cheng, "Humanoid multimodal tactile-sensing modules," *IEEE Transactions on Robotics*, vol. 27, no. 3, pp. 401–410, 2011.

23. P. Maiolino, A. Ascia, M. Maggiali, L. Natale, G. Cannata, and G. Metta, "Large scale capacitive skin for robots," in *Smart Actuation and Sensing Systems* (G. Berselli, R. Vertechy, and G. Vassura, eds.), ch. 8, Rijeka: IntechOpen, 2012.

24. L. Chen, X. Chang, H. Wang, J. Chen, and Y. Zhu, "Stretchable and transparent multimodal electronic-skin sensors in detecting strain, temperature, and humidity," *Nano Energy*, vol. 96, p. 107077, 2022.

25. A. Georgopoulou, D. Hardman, T. G. Thuruthel, F. Iida, and F. Clemens, "Sensorized skin with biomimetic tactility features based on artificial cross-talk of bimodal resistive sensory inputs," *Advanced Science*, vol. n/a, no. n/a, p. 2301590.

26. Z. Yuan and G. Shen, "Materials and device architecture towards a multimodal electronic skin," *Materials Today*, 2023.

27. S. Shimadera, K. Kitagawa, K. Sagehashi, Y. Miyajima, T. Niiyama, and S. Sunada, "Speckle-based high-resolution multimodal soft sensing," *Scientific Reports*, vol. 12, no. 1, p. 13096, 2022.

28. T. G. Thuruthel, J. Hughes, A. Georgopoulou, F. Clemens, and F. Iida, "Using redundant and disjoint time-variant soft robotic sensors for accurate static state estimation," *IEEE Robotics and Automation Letters*, vol. 6, no. 2, pp. 2099–2105, 2021.

29. I. Andrussow, H. Sun, K. J. Kuchenbecker, and G. Martius, "Minsight: A fingertip-sized vision-based tactile sensor for robotic manipulation," *Advanced Intelligent Systems*, vol. 5, no. 8, p. 2300042, 2023.

30. B. Ward-Cherrier, N. Pestell, L. Cramphorn, B. Winstone, M. E. Giannaccini, J. Rossiter, and N. F. Lepora, "The tactip family: Soft optical tactile sensors with 3d-printed biomimetic morphologies," *Soft robotics*, vol. 5, no. 2, pp. 216–227, 2018.

31. K. Park, H. Yuk, M. Yang, J. Cho, H. Lee, and J. Kim, "A biomimetic elastomeric robot skin using electrical impedance and acoustic tomography for tactile sensing," *Science Robotics*, vol. 7, no. 67, p. eabm7187, 2022.

32. H. Alirezaei, A. Nagakubo, and Y. Kuniyoshi, "A highly stretchable tactile distribution sensor for smooth surfaced humanoids," in *2007 7th IEEE-RAS International Conference on Humanoid Robots*, pp. 167–173, 2007.

33. Y. Zhang, G. Laput, and C. Harrison, "Electrick: Low-cost touch sensing using electric field tomography," in *Proceedings of the 2017 CHI Conference on Human Factors in Computing Systems*, CHI '17, (New York, NY, USA), p. 1–14, Association for Computing Machinery, 2017.

34. K. Liu, Y. Wu, S. Wang, H. Wang, H. Chen, B. Chen, and J. Yao, "Artificial sensitive skin for robotics based on electrical impedance tomography," *Advanced Intelligent Systems*, vol. 2, no. 4, p. 1900161, 2020.

35. X. Duan, S. Taurand, and M. Soleimani, "Artificial skin through super-sensing method and electrical impedance data from conductive fabric with aid of deep learning," *Scientific reports*, vol. 9, no. 1, pp. 8831–11, 2019.

36. A. Costa Cornellà, D. Hardman, L. Costi, J. Brancart, G. Van Assche, and F. Iida, "Variable sensitivity multimaterial robotic e-skin combining electronic and ionic conductivity using electrical impedance tomography," *Scientific Reports*, vol. 13, p. 20004, Nov 2023.

37. H. Lee, K. Park, J. Kim, and K. J. Kuchenbecker, "Internal array electrodes improve the spatial resolution of soft tactile sensors based on electrical resistance tomography," in *2019 International Conference on Robotics and Automation (ICRA)*, pp. 5411–5417, 2019.

38. M. Cheney, D. Isaacson, and J. C. Newell, "Electrical impedance tomography," *SIAM review*, vol. 41, no. 1, pp. 85–101, 1999.

39. K. Park, H. Lee, K. J. Kuchenbecker, and J. Kim, "Adaptive optimal measurement algorithm for ert-based large-area tactile sensors," *IEEE/ASME Transactions on Mechatronics*, vol. 27, no. 1, pp. 304–314, 2022.

40. S. Wang and Z. Sun, "Hydrogel and machine learning for soft robots' sensing and signal processing: A review," *Journal of bionics engineering*, vol. 20, no. 3, pp. 845–857, 2023.

41. A. Adler, P. O. Gaggero, and Y. Maimaitijiang, "Adjacent stimulation and measurement patterns considered harmful," *Physiological measurement*, vol. 32, no. 7, pp. 731–744, 2011.

42. C. Xu, X. Dong, X. Shi, F. Fu, W. Shuai, R. Liu, and F. You, "Comparison of drive patterns for single current source eit in computational phantom," in *2008 2nd International Conference on Bioinformatics and Biomedical Engineering*, pp. 1500–1503, 2008.

43. O. Luppi Silva, R. Gonzalez Lima, T. Castro Martins, F. Silva de Moura, R. Seiji Tavares, and M. Sales Guerra Tsuzuki, "Influence of current injection pattern and electric potential measurement strategies in electrical impedance tomography," *Control Engineering Practice*, vol. 58, pp. 276–286, 2017.

44. H. Wang, G. Xu, S. Zhang, and W. Yan, "Optimized excitation mode for generalized back projection algorithm in 3-d eit," *IEEE Transactions on Magnetics*, vol. 51, no. 3, pp. 1–4, 2015.

45. S. Russo, S. Nefti-Meziani, N. Carbonaro, and A. Tognetti, "A quantitative evaluation of drive pattern selection for optimizing eit-based stretchable sensors," *Sensors*, vol. 17, no. 9, 2017.

46. W. R. Lionheart, K. Paridis, and A. Adler, "Resistor networks and transfer resistance matrices," in *Proc. of the 13th Int. Conf. on Biomedical Applications of Electrical Impedance Tomography (Tianjin, China 23–25 May 2012)*, 2012.

47. H. Zhang, A. Kalra, A. Lowe, Y. Yu, and G. Anand, "A hydrogel-based electronic skin for touch detection using electrical impedance tomography," *Sensors*, vol. 23, no. 3, 2023.

48. M. Abdelwahed, L. Zerioul, A. Pitti, and O. Romain, "Using novel multi-frequency analysis methods to retrieve material and temperature information in tactile sensing areas," *Sensors*, vol. 22, no. 22, 2022.

49. D. Hardman, T. G. Thuruthel, and F. Iida, "Tactile perception in hydrogel-based robotic skins using data-driven electrical impedance tomography," *Materials Today Electronics*, vol. 4, p. 100032, 2023.

50. F. Pennati, A. Angelucci, L. Morelli, S. Bardini, E. Barzanti, F. Cavallini, A. Conelli, G. Di Federico, C. Paganelli, and A. Aliverti, "Electrical impedance tomography: From the traditional design to the novel frontier of wearables," *Sensors*, vol. 23, no. 3, 2023.

51. Y. Zhang and C. Harrison, "Tomo: Wearable, low-cost electrical impedance tomography for hand gesture recognition," in *Proceedings of the 28th Annual ACM Symposium on User Interface Software & Technology*, UIST '15, (New York, NY, USA), p. 167–173, Association for Computing Machinery, 2015.

52. D. Hardman, T. George Thuruthel, and F. Iida, "Self-healing ionic gelatin/glycerol hydrogels for strain sensing applications," *NPG Asia materials*, vol. 14, no. 1, 2022.

53. K. Paulson, W. Lionheart, and M. Pidcock, "Optimal experiments in electrical impedance tomography.," *IEEE Transactions on Medical Imaging*, vol. 12, no. 4, pp. 681–686, 1993.

54. S. L. Brunton, J. Nathan Kutz, K. Manohar, A. Y. Aravkin, K. Morgansen, J. Klemisch, N. Goebel, J. Buttrick, J. Poskin, A. W. Blom-Schieber, *et al.*, "Data-driven aerospace engineering: reframing the industry with machine learning," *AIAA Journal*, vol. 59, no. 8, pp. 2820–2847, 2021.

55. M. Soori, B. Arezoo, and R. Dastres, "Artificial intelligence, machine learning and deep learning in advanced robotics, a review," *Cognitive Robotics*, 2023.

56. S. Tian, F. Ebert, D. Jayaraman, M. Mudigonda, C. Finn, R. Calandra, and S. Levine, "Manipulation by feel: Touch-based control with deep predictive models," in *2019 International Conference on Robotics and Automation (ICRA)*, pp. 818–824, IEEE, 2019.

57. J. Zhu, J. C. Snowden, J. Verdejo, E. Chen, P. Zhang, H. Ghaednia, J. H. Schwab, and S. Mueller, "Eit-kit: An electrical impedance tomography toolkit for health and motion sensing," in *The 34th Annual ACM Symposium on User Interface Software and Technology*, UIST '21, (New York, NY, USA), p. 400–413, Association for Computing Machinery, 2021.

58. A. Adler and W. R. B. Lionheart, "Uses and abuses of eidors: an extensible software base for eit," *Physiological measurement*, vol. 27, no. 5, pp. S25–S42, 2006.

59. T. Someya, T. Sekitani, S. Iba, Y. Kato, H. Kawaguchi, and T. Sakurai, "A large-area, flexible pressure sensor matrix with organic field-effect transistors for artificial

skin applications," *Proceedings of the National Academy of Sciences*, vol. 101, no. 27, pp. 9966–9970, 2004.

60. Q. Hua, J. Sun, H. Liu, R. Bao, R. Yu, J. Zhai, C. Pan, and Z. L. Wang, "Skin-inspired highly stretchable and conformable matrix networks for multifunctional sensing," *Nature communications*, vol. 9, no. 1, p. 244, 2018.

61. S. Sundaram, P. Kellnhofer, Y. Li, J.-Y. Zhu, A. Torralba, and W. Matusik, "Learning the signatures of the human grasp using a scalable tactile glove," *Nature*, vol. 569, no. 7758, pp. 698–702, 2019.

62. W. W. Lee, Y. J. Tan, H. Yao, S. Li, H. H. See, M. Hon, K. A. Ng, B. Xiong, J. S. Ho, and B. C. Tee, "A neuro-inspired artificial peripheral nervous system for scalable electronic skins," *Science Robotics*, vol. 4, no. 32, p. eaax2198, 2019.

63. D. Hu, F. Giorgio-Serchi, S. Zhang, and Y. Yang, "Stretchable e-skin and transformer enable high-resolution morphological reconstruction for soft robots," *Nature Machine Intelligence*, vol. 5, no. 3, pp. 261–272, 2023.

64. D. Zhong, C. Wu, Y. Jiang, Y. Yuan, M.-g. Kim, Y. Nishio, C.-C. Shih, W. Wang, J.-C. Lai, X. Ji, *et al.*, "High-speed and large-scale intrinsically stretchable integrated circuits," *Nature*, vol. 627, no. 8003, pp. 313–320, 2024.

65. L. Nicholls, D. Hardman, and F. Iida, "Multi-touch recognition of hydrogel-based e-skins using real-world eit datasets," in *2024 IEEE 7th International Conference on Soft Robotics (RoboSoft)*, pp. 103–108, 2024.

# Acknowledgments

**Funding:** Supported by the Samsung Global Research Outreach Program (GRO G118293), the Royal Society research grant RGS\R1\231472, and by EPSRC DTP EP/R513180/1.
**Author contributions:** All authors conceptualized the study and wrote the paper. D.H. performed all fabrication and experiments. D.H. and T.G. performed the data analysis. D.H. created the figures. **Data and materials availability:** All other data needed to evaluate the conclusions in the paper are present in the paper or the Supplementary Materials. The data for this study have been deposited in the databases `https://doi.org/10.5281/zenodo.15387404` and `https://github.com/DSHardman/InfoStructuring`.

# Figures and Tables

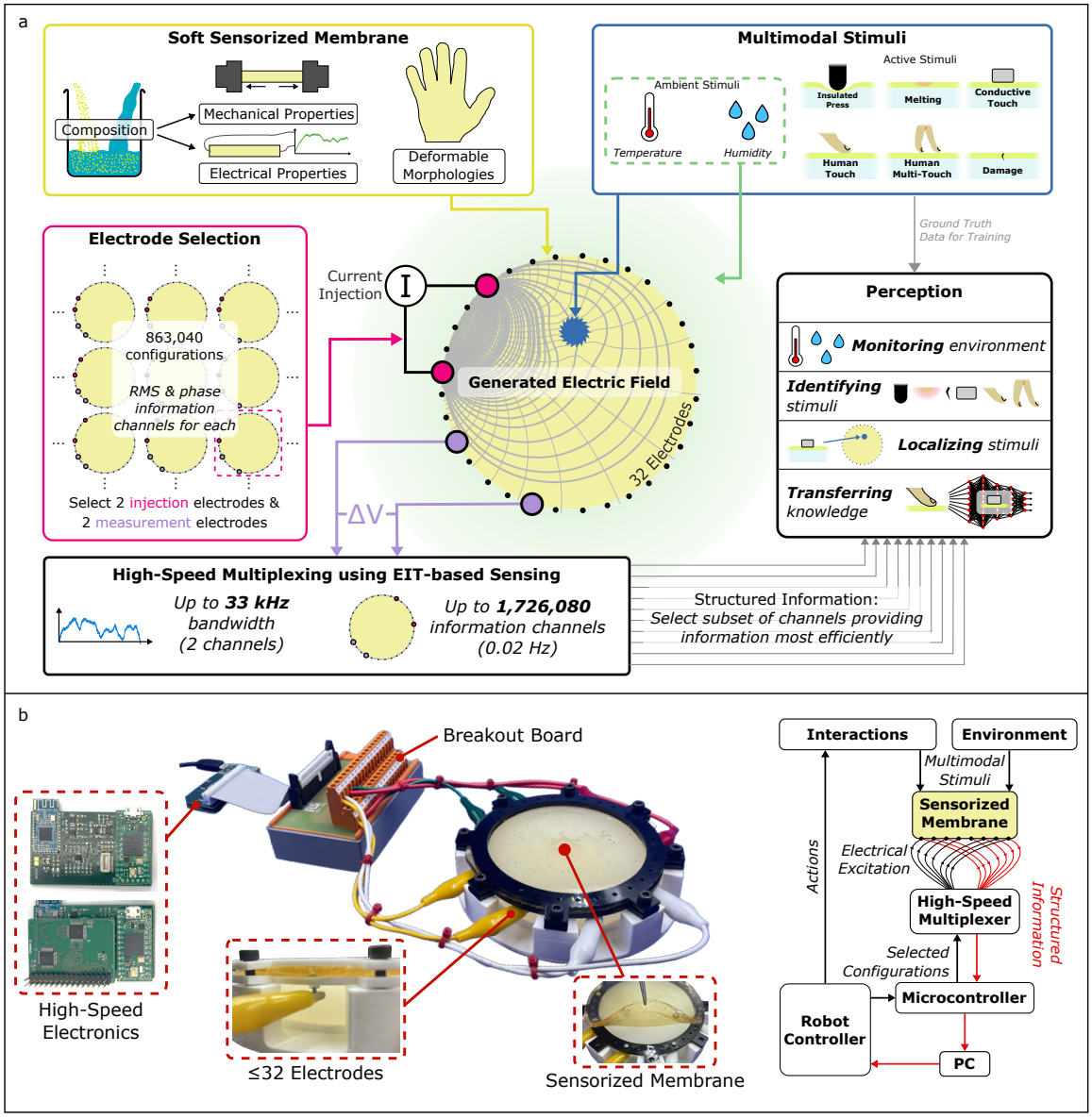



Figure 1: **Multimodal information structuring of a soft sensorized skin**. (**a**) Multimodal stimuli are detected through the generation of an electric field across the skin using EIT hardware: the information which this returns can be structured through the skin's own composition and morphology, and through the configuration of excitation electrodes. This work uses a gelatin-based hydrogel as its soft membrane, since this can straightforwardly be cast into complex continuous shapes which contain no soft-rigid interfaces, such as a human-scale hand. By selectively exciting the membrane, structured information is output, which can be used to monitor environmental conditions, localize tactile stimuli, and explore the similarities and differences between multimodal stimuli. (**b**) The 8-electrode hydrogel membrane used for initial tests: high-speed electronics connected to the membrane's perimeter enable the comparison of all 1680 possible electrode configurations. A 10 cm circular membrane is fabricated, which is used to detect all the ambient and active stimuli presented in (a). In a fully-implemented system, this data would be fed directly to the robot's controller.

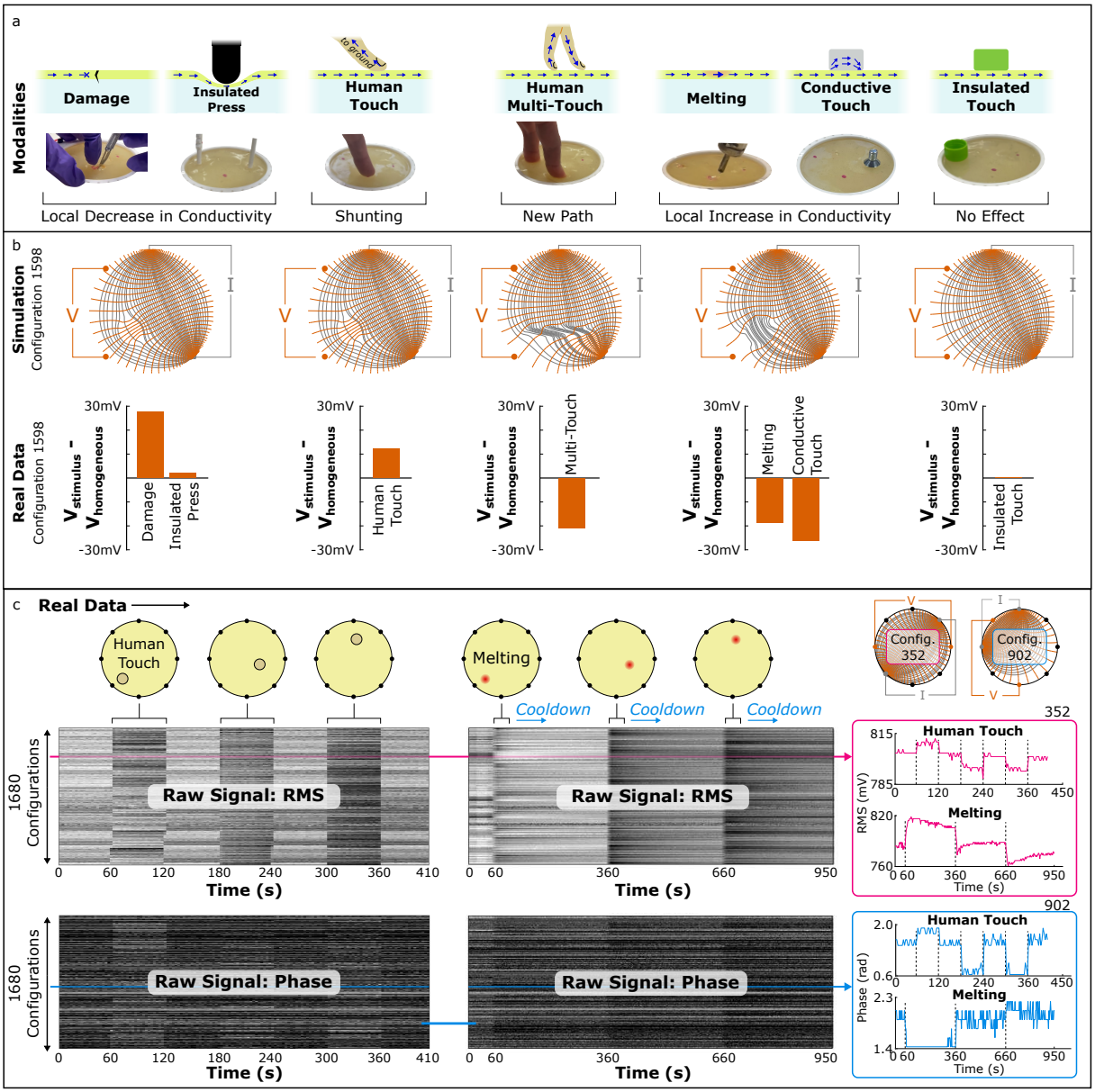



Figure 2: **Detecting multimodal stimuli using a generated electric field**. (**a**) The seven modalities under consideration, and their mechanisms of local conductivity impact on a soft hydrogel skin. Damage/Insulated Press and Melting/Conductive Touch modalities are grouped in pairs due to their similar mechanisms. (**b**) The effect of these mechanisms on one EIT-based tetrapolar electrode configuration around the 8-electrode circular skin. Simulations map the expected electric field in the presence of each stimulus, with bar graphs showing the measured responses when the seven modalities are applied to Figure 1b's circular skin. (**c**) Raw responses from all 1680 electrode configurations for three differently-located human touch and melting modalities. Each horizontal line plots the response of a single electrode configuration, normalized to fall within the range [0, 1]. The raw time series responses of two configurations (numbered 352 and 902 in the 1680 full configuration sweep) are plotted over the same period.

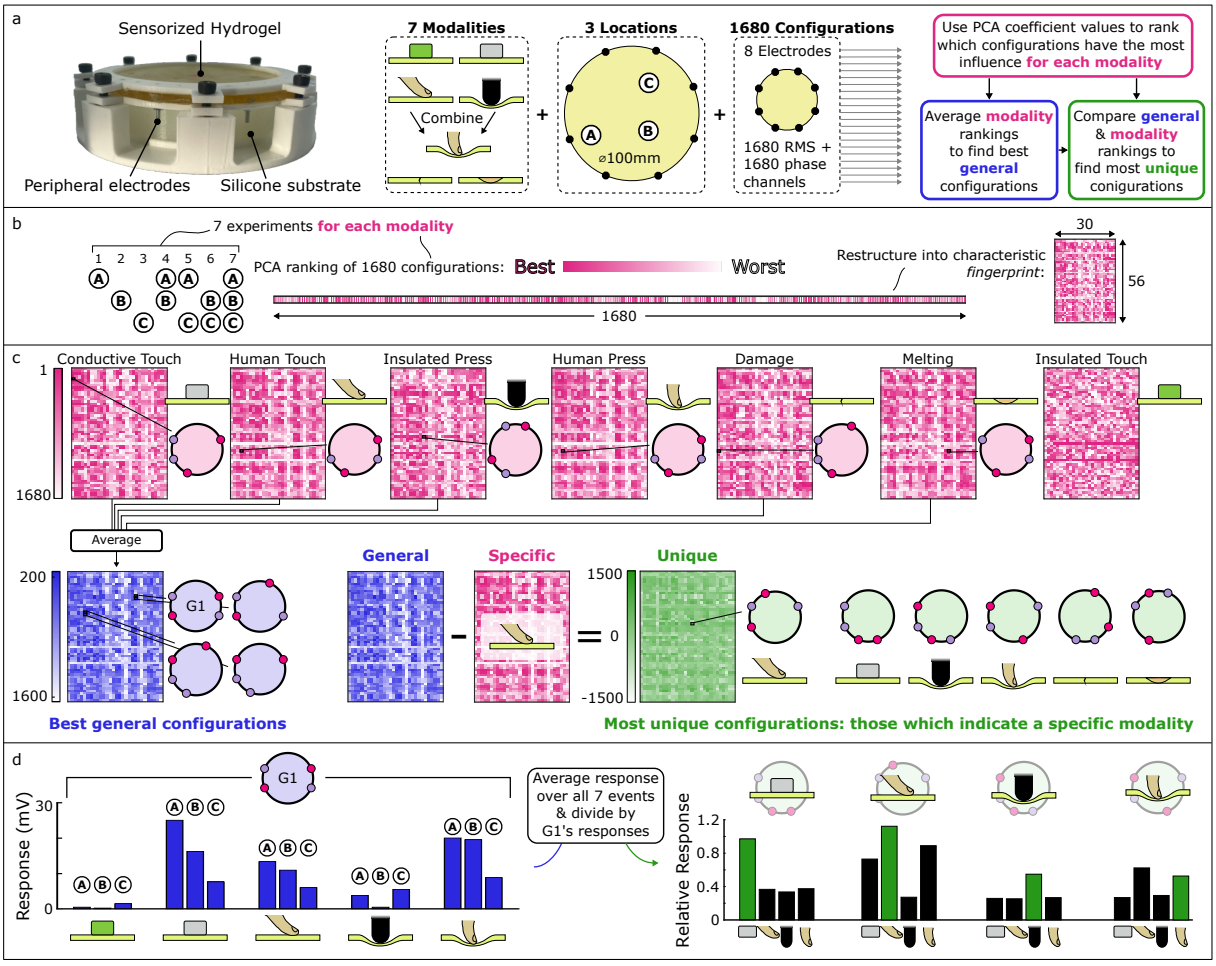



Figure 3: **Empirically identifying which configurations return the most valuable information to enable multimodal perception**. (**a**) 7 modalities are used to stimulate the circular skin at three locations, while all 1680 electrode configurations are monitored. By ranking and comparing the responses, optimal configurations can be identified. (**b**) The generation of characteristic 'fingerprints' for each modality, based on the absolute PCA coefficients of the 1680 configurations' RMS magnitudes. Insulated touch does not return a structured fingerprint, due to the membrane's inability to respond to this modality. (**c**) Using the fingerprints to identify the configurations which have the most influence for each modality, regardless of modality (referred to as the 'general' case), and which generate a response most unique to each modality. (**d**) Response magnitudes using the best general configuration G1: these vary with modality and with location. Relative responses for four unique configurations are also plotted: as designed, these give the strongest response for their particular modality. Human touch and human press modalities appear most difficult to decouple.

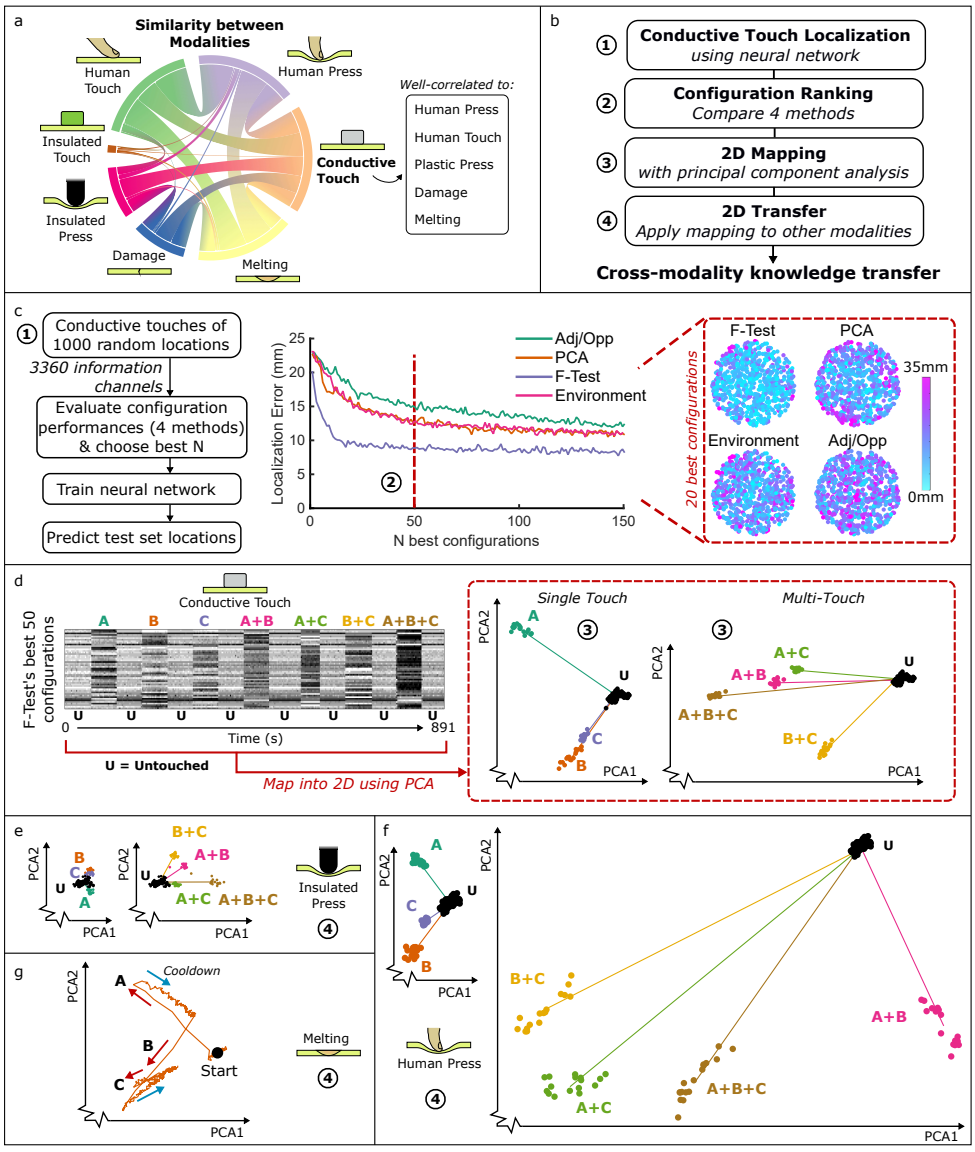



Figure 4: **Transferring localization knowledge to unseen modalities**. (**a**) Similarities between the modalities, based on the coefficients of their first principal component: conductive touch is selected for transferability tests due to its high similarity to all other modalities. (**b**) The process of cross-modality knowledge transfer: a neural network is trained to localize conductive touch stimuli, and the key configurations identified: these are used to visualize the responses of other modalities. (**c**) Four configuration-ranking methods are compared in structuring the input to a neural network which localizes 1000 conductive touches at random locations. When examining the convergence rates and distribution maps of localization errors on a 10% test set, statistical F-Test rankings perform best and are selected for cross-modality transfers. (**d**) F-Test's best 50 configurations are used to map the responses into a 2D plane through principal component analysis (PCA) where different stimulus locations can be visualized. Multi-touch vectors can be superposed from single touch vectors. (**e**) The same mapping is applied to insulated press, which gives smaller response vectors in the opposite direction. (**f**) The mapping is applied to human presses, which behaves similarly for single locations, and responds very strongly to multi-location presses due to Figure 2a's new mechanism. (**g**) The mapping is applied to the localized melting time series to produce a parametric plot (Video S1), with response vectors in the same direction as conductive touch due to their shared response mechanism.




Figure 5: **Application to 3D skins: design of a hollow hand**. (**a**) A hollow skin is cast from the sensorized hydrogel, with 32 electrodes positioned around its wrist. The hand's entire surface is continuous and contains no soft/rigid interfaces. 863,040 electrode configurations are available to detect multimodal stimuli. In addition to the modalities already considered, a new proprioceptive response is possible when the fingers bend. (**b**) Fabrication steps of the skin. Positive inserts are used to create the hollow membrane, with all 32 electrodes being routed into a ribbon cable at the hand's base to connect to EIT hardware. A full description of the process is given in the supplementary material.

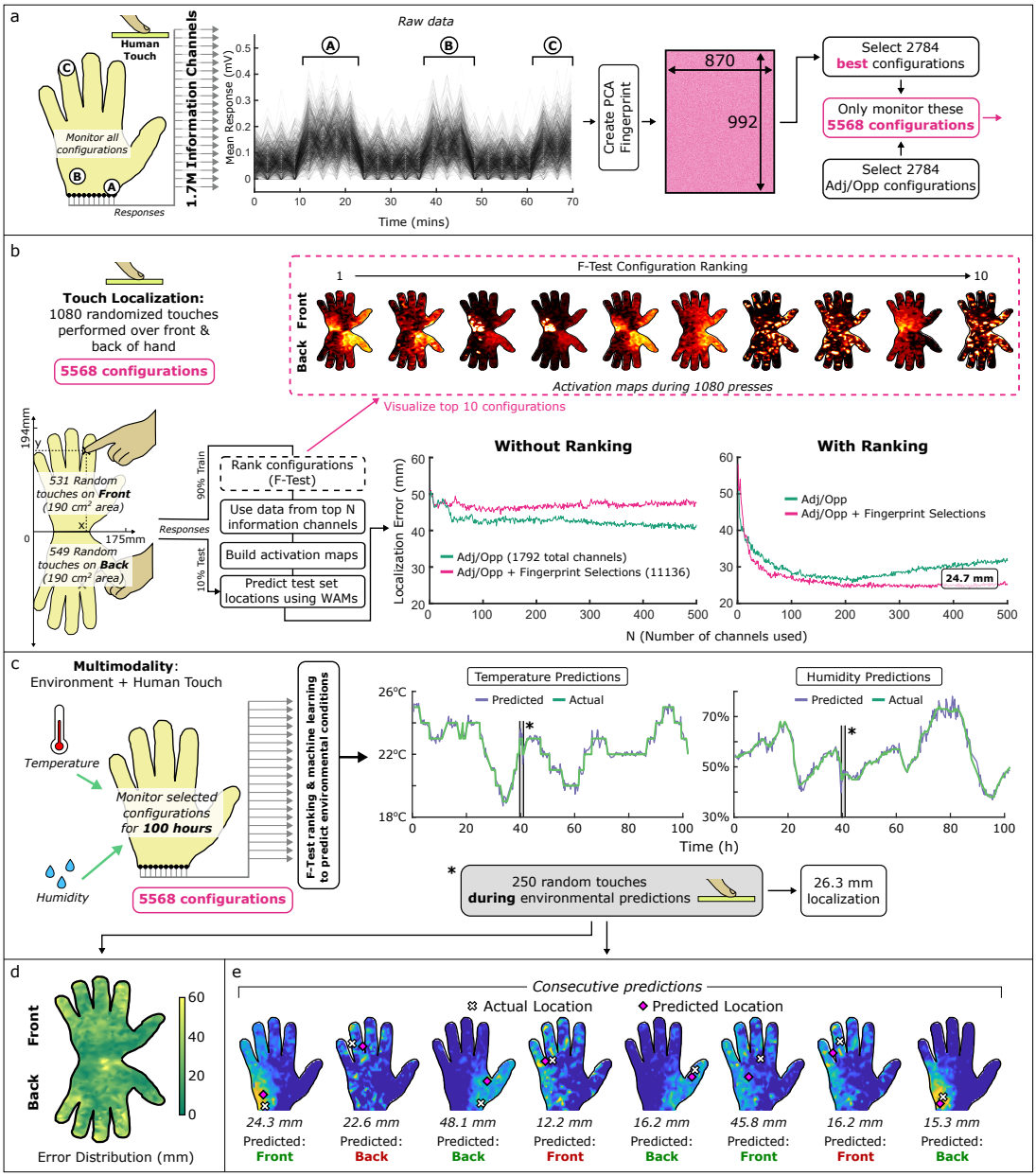



Figure 6: **Structuring information to predict multimodal stimuli in the 3D hand**. (**a**) Even with the electrodes at the wrist, tactile responses are still seen in the setup's 1,726,080 information channels. Fingerprinting is used to select which should be monitored. **(b)** Using F-test ranking to improve the efficiency of tactile localization. 1080 randomized light touches over the front and back of the hand are predicted using the WAMs method: using N channels, the average localization errors of a 10% test set are plotted. Activation maps of the 10 top-ranked configurations are shown, which respond to touches in different areas of the hand. **(c)** Using F-Test to select the channels, accurate predictions of environmental temperature and humidity for a 10% test set can be learned by a neural network, while touches are taking place. **(d)** Error distributions over the front and back of the hand. **(e)** Eight test set predictions from the multimodal measurements.

Citations from supplementary material: (*30, 31, 36, 46, 58–65*)